doi:10.26443/seismica.v2i4.1701

SEISMICA

The Distribution of Interseismic Locking on the Cascadia Subduction Zone Using Bayesian Methods

Anna E. R. Pearson [1], **David A. Schmidt** [1]

[1]Department of Earth and Space Sciences, University of Washington, Seattle, USA

Author contributions: *Conceptualization*: A. Pearson, D. Schmidt. *Data Curation*: A. Pearson. *Funding Acquisition*: D. Schmidt. *Investigation*: A. Pearson. *Methodology*: A. Pearson, D. Schmidt. *Software*: A. Pearson. *Supervision*: D. Schmidt. *Writing – original draft*: A. Pearson. *Writing – review & editing*: A. Pearson, D. Schmidt.

Production Editor: Alice Gabriel
Handling Editor: Alice Gabriel
Copy & Layout Editor: Mengjie Zheng

Signed reviewer(s): Kaj M. Johnson

Received: April 22, 2025
Accepted: August 16, 2026
Published: August 31, 2026

Abstract We use a Bayesian probabilistic framework to invert for the kinematic locking distribution on the Cascadia Subduction Zone, constrained by surface deformation data and a prior assumption of the locking pattern. Interseismic surface deformation observations include land and seafloor GNSS data, along with decades-averaged vertical rates from spirit leveling. Using a Bayesian inversion framework, we explore a range of priors, including different updip and downdip limits and along-strike heterogeneity in locking. Data corrections account for contemporary glacial isostatic adjustment and viscoelastic effects. The mean of the locking distributions suggests a highly coupled offshore zone, transitioning to creep at a depth that varies along strike, with sensitivity to the prior. The shape of the locking distributions varies along strike, with the highest means near the deformation front and in Central Oregon. Results suggest high probability of strong locking offshore and low locking deeper than 20 km depth, which can provide insight into associated hazards. This work also highlights the importance of tradeoffs among different deformation signals. We find that the combined influence of viscoelasticity and glacial isostatic adjustment is relatively small in Cascadia, on the order of a few mm/yr vertically, indicating that elastic strain accumulation dominates the contemporary crustal deformation.

Non-technical summary We study how strain builds up along the Cascadia Subduction Zone, a major offshore fault that poses significant earthquake and tsunami risks. Using probabilistic methods and surface motion data from land and seafloor GNSS stations, we estimate where the fault is locked (stuck and accumulating strain) and where it is creeping slowly. We also account for other factors affecting surface motion, such as land rebounding from glaciation and the slow relaxation of stress in the upper mantle. Our results suggest that the offshore portion of the fault is mostly locked, meaning it is storing energy for a future earthquake. This locked area varies along the coast and becomes more uncertain near the offshore edge of the fault. We find that the impact of glacial rebound and deep relaxation of stress on our measurements is relatively small, so most of the surface movement can be attributed to the buildup of elastic strain. These findings improve our understanding of where strain is accumulating, which can inform future hazards.

1 Introduction

1.1 Locking in Cascadia

An estimate of fault locking, calculated by inverting observed surface deformation, can provide a valuable constraint on where strain is currently accumulating along a plate boundary and a proxy for where a future earthquake might rupture. In this paper, we define locking kinematically, where "locked" means where the fault is not slipping. An alternative definition, not used in this paper, is to define locking where "locked" is based on the Amontons-Coulomb static frictional regime creating a region of zero sliding (Sato et al., 2025). Historically, many past megathrust earthquakes have ruptured along patches identified as locked zones, such as the 2007 M_w 8.4 Bengkulu, 2011 M_w 9.1 Tohoku, and 2012 M_w 7.6 Nicoya earthquakes, revealing a strong correlation between the locking pattern and coseismic slip (Konca et al., 2008; Loveless and Meade, 2011; Protti et al., 2013). This underscores the importance of understanding the locking state for seismic hazard assessments. However, we cannot assume an exact prediction of the future coseismic slip pattern, as coseismic slip does not always mirror the prior locking pattern. For example, a highly locked seismic gap was identified from geodetic observations prior to the 2010 M_w 8.8 Maule earthquake. While the earthquake slip did occur in relatively highly locked areas, large areas of high locking did not slip, and correlation between locking and coseismic slip was poor (Lorito et al., 2011). Despite not serving as a strong predictor of the coseismic slip distribution, low locking zones align well with regions of rupture arrest for several earthquakes in Chile, including the Maule earthquake (Métois et al., 2012). An analysis of the slip history on the Sunda subduction zone found that the area of coseismic slip better correlated with an estimate of the stress state as a result of both prior earthquakes and the interseismic locking pattern (Nalbant

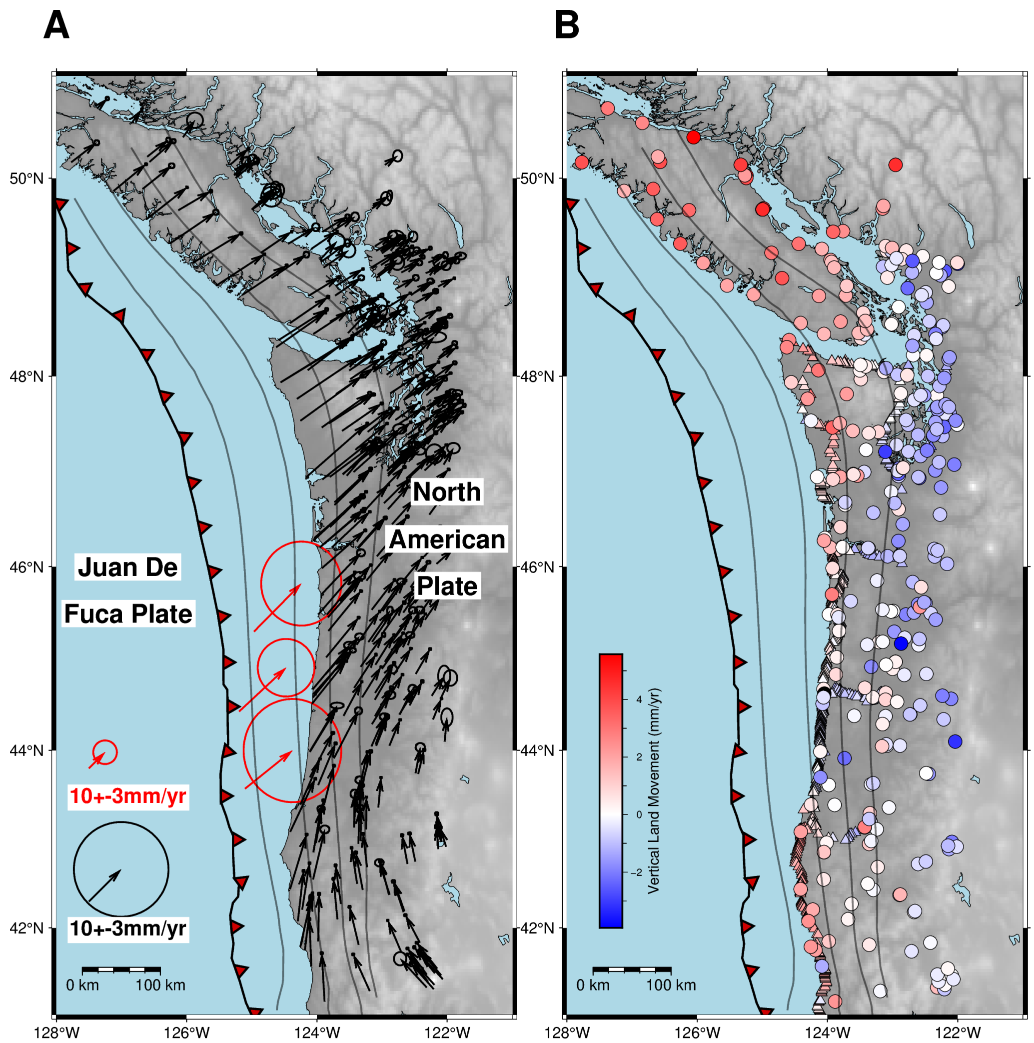

Figure 1 Map of Cascadia, with the trace of the plate boundary and 10 km interval contours to the depth of the subducting slab (grey lines, 10km-40km) (Carbotte et al., 2024; McCrory et al., 2012). (A) Black arrows showing horizontal velocities of GNSS stations (Blewitt et al., 2018; Jamason et al., 2004; Miller et al., 1997; Zumberge, 1999). (b) Circles (GNSS stations) and triangles (leveling) showing vertical velocity (Blewitt et al., 2018; Jamason et al., 2004; Newton et al., 2021; Patton et al., 2023; Miller et al., 1997; Zumberge, 1999).

et al., 2013). Although it cannot provide a direct prediction, locking does provide a first-order assessment of the pattern of slip deficit and indicates areas of possible future coseismic slip.

The Cascadia Subduction Zone is characterized by subduction of the Juan de Fuca Plate beneath the North American Plate (Fig. 1), at a rate of about 30-40 mm per year. Paleoseismic records point to a significant seismic and tsunamigenic hazard, most recently with the 1700 earthquake (Satake et al., 1996). Low levels of seismicity and geodetic velocities aligned with the movement of the Juan De Fuca Plate indicate locking along the subduction zone, thus suggesting that the system is currently accumulating strain during the interseismic phase of the earthquake cycle before the next major earthquake (e.g. Li et al., 2018; McCaffrey et al., 2013; Schmalzle et al., 2014; Sherrill et al., 2024; Pollitz, 2025). An improved understanding of this locking is therefore important for assessment of the ongoing tectonic processes.

Geodetic estimates of the locking pattern are particularly instructive in Cascadia, as there are few alternative ways of assessing likely future rupture potential. The last major interplate earthquake and tsunami occurred in 1700 with limited paleoseismic data with which to estimate the rupture zone (Kemp et al., 2018; Satake et al., 1996; Wirth and Frankel, 2019; Wang et al., 2013). Seismicity rates are currently low, likely because the modern period of recorded earthquakes falls entirely within the interseismic period of the earthquake cycle. As a result, the long-term seismic moment release rate may be underestimated using only contemporary seismicity rates.

1.2 Complicating factors

When interpreting the observed surface deformation for fault locking, several additional factors and signals need to be considered. The asthenosphere deforms viscoelastically during the earthquake cycle, meaning that while it can still respond elastically there is also a delayed viscous response creating a decaying time-dependent signal. This occurs both in the postseismic period, during which the viscoelastic relaxation dominates in response to the coseismic stress and afterslip, as well as in the interseismic period, during which there is concurrent but diminished viscoelastic relaxation of the (Pollitz, 2025; Wang et al., 2012). Leveling data from the Nankai subduction zone provide some evidence of a vertical deformation pattern on land that changes over time, indicating postseismic viscoelastic relaxation in the mantle (Li et al., 2020; Thatcher, 1984; Wang and Tréhu, 2016). The Cascadia Subduction Zone is currently in a late interseismic stage, 325 years since the last major earthquake, meaning that a time-dependent postseismic signal has largely faded. However, the effect of relaxation of the ongoing strain accumulation is more pronounced and this can lead to a wider area of inland deformation than would be expected with an elastic model (Wang et al., 2012). Solely using modern geodetic data, within the late stage of the seismic cycle, also means that asperities on which strain accumulated early in the earthquake cycle may be missed as possible zones of coseismic slip. Observations of full earthquake cycles are limited within the seismic record, making it difficult to assess how much locking rates may vary over the seismic cycle.

In Cascadia and many other regions, several additional processes are impacting the surface deformation field. Local deformation may result from crustal faults, in contrast with the large regional signal from elastic locking on the subduction zone. Additionally, a lobe of the Cordilleran ice sheet during the last glacial period covered part of the Cascadia region, extending just south of the Puget Sound (Clark et al., 2019). Since deglaciation, this region has experienced glacial isostatic adjustment, in which there is deformation in response to the changing surface load. This effect decreased over time but continues to affect velocities to this day, especially in the vertical direction, although there is some debate as to its relative magnitude (Engelhart et al., 2015; Newton et al., 2021; Yousefi et al., 2021). Seasonal surface loading from precipitation and snowpack introduces short-term deformation signals, which are largely averaged out when calculating long-term surface velocities. Groundwater withdrawal and compaction may also lead to pronounced subsidence, with spatial biases seen on short spatial scales or at individual stations. This effect is more prominent outside the Pacific Northwest, where groundwater withdrawal is more common (Clark et al., 2019; Shirzaei et al., 2020). Eliminating those additional signals in the surface deformation allows for improved estimates of elastic locking in Cascadia.

Limited data resolution presents an additional challenge, particularly with offshore portions of the megathrust that are poorly resolved by the data from onshore stations. The potential presence of shallow locking has important implications for tsunami hazards. Accumulated strain close to the deformation front increases the potential for coseismic slip extending to the deformation front, and associated larger tsunami amplitude (Lindsey et al., 2021; Wang and Tréhu, 2016). Limited seafloor geodetic coverage impedes full resolution of the updip locking pattern.

1.3 Probabilistic approaches

Locking models that fit the data in Cascadia are not unique, as they are derived from an inverse problem in which there are insufficient data and model design to create a unique solution (e.g. Li et al., 2018; McCaffrey et al., 2013; Schmalzle et al., 2014). Fault locking models can vary in updip and downdip locking limits, and may or may not include the presence of specific highly locked areas, such as the zone immediately offshore the Olympic Peninsula. The absence of a clear assessment of a unique superior model calls for a probabilistic approach to characterizing the locking pattern.

Bayesian inversion methods encompass a range of inversion algorithms that support a probabilistic assessment of locking (Minson et al., 2013). They incorporate both a prior, providing physical bounds based on *a priori* information about the problem, and an observational dataset. The inversion output depends on the model resolution and the uncertainty of the dataset. Previous studies have successfully utilized Bayesian approaches to constrain locking and slip patterns in areas with limited data (Dal Zilio et al., 2020; Minson et al., 2014; Wang et al., 2012; Matsu'ura et al., 2007). These have largely involved Monte Carlo Markov Chain (MCMC)-based approaches, including CATMIP (Dal Zilio et al., 2020; Minson et al., 2014; Sherrill et al., 2024; Wang et al., 2012) and maximum likelihood algorithms (Matsu'ura et al., 2007), which involves an iterative search to select the best model from a series. The CATMIP algorithm does not require any simplifying assumptions in creating the model, and the algorithm characterizes the complete Bayesian posterior distribution (Minson et al., 2013). In comparison with the basic Metropolis algorithm, CATMIP's use of resampling and transitioning allows it to more efficiently explore the full parameter space (Minson et al., 2013). Our elastic Bayesian model explores full probability distributions of locking along the fault that are consistent with the data and prior constraints on the locking pattern. This approach recognizes the limitations of available geodetic data in the region, offering a probabilistic view of potential locking scenarios.

2 Data and Methods

To assess the locking pattern, we develop an interseismic locking model that is constrained by three-component surface velocities from GNSS and vertical surface velocities from spirit leveling. We apply approximative corrections to the data to account for forearc rotation, as well as possible contributions from glacial isostatic rebound and viscoelastic deformation. We construct an associated data covariance matrix and calculate a set of Green's functions defining the relationship between the surface deformation dataset and fault locking along the plate interface. We then run a Bayesian inversion algorithm to estimate the distribution of locking for each fault element.

2.1 Data

The three-dimensional geometry of the subduction zone interface is defined using the model of Bloch et al. (2023). We modify the shallow geometry to better merge with the newly acquired geometry from the CASIE21 project (Bloch et al., 2023; Carbotte et al., 2024). The fault is discretized into a triangular mesh with 40 km length sides using the program *Cubit* (Coreform LLC, 2018).

We create our surface velocity dataset (Fig. 1) by amalgamating GNSS data from multiple processing centers following the methodology of Newton et al. (2021). These include processing center velocity solutions from continuous land-based GNSS sites (Blewitt et al., 2018; Jamason et al., 2004; Miller et al., 1997; Zumberge, 1999), repeated leveling surveys (Newton et al., 2021; Patton et al., 2023), and newly analyzed seafloor GNSS-A sites (DeSanto et al., 2025). Three-component land-based GNSS velocities are generated by calculating a mean velocity at each station with associated propagated uncertainty based on the results from the four processing centers and applying a shift to the leveling measurements in order to bring them into the same vertical frame of reference as the GNSS stations (see Newton et al., 2021).

Building upon the original dataset created in Newton et al., we expand southward from a latitude of 45° N to 41° N and add horizontal velocities to the analysis using the same methodology. In addition, we refine the dataset by excluding GNSS stations with high uncertainty or a greater than 40° mismatch in the azimuth of the estimated velocity in comparison with the surrounding stations. We remove stations located close to active volcanoes and notable outliers. For example, we eliminate GNSS station V096, a station with a much higher velocity that could indicate confounding local factors impacting the data, such as compaction. The refined velocity dataset is archived on Zenodo (see Data and Code Availability).

2.2 Data Corrections

We include several corrections to the data used to constrain the model, including a correction for forearc rotation, glacial isostatic adjustment (GIA), and viscoelasticity of the upper mantle. The Cascadia forearc has been undergoing clockwise rigid body rotation for at least the last 16 Myr, with minimal internal strain within the forearc itself (Savage et al., 2000; Wells and McCaffrey, 2013). We correct horizontal velocities within the forearc based on a rotation rate with the pole located at 45.16°N latitude, -119.01°W longitude, applying the correction at stations south of a latitude of 46°N (McCaffrey et al., 2007). Therefore, the resulting velocities record the motion of the Juan de Fuca Plate relative to a stable forearc in Oregon and northern California, instead of relative to the North American plate. We also test the rotation rate as a model element in the inversion, using either the same or an optimized pole location.

Isostatic adjustment in response to the last glacial period continues to this day in the Cascadia region, in which there is uplift under formerly glaciated regions and subsidence under the former glacial forebulge. We account for uplift and subsidence driven by GIA using a set of models (Yousefi et al., 2021) that predict modern GIA given different possible viscosity and lithospheric thickness models of the earth. Among the set of possible models presented in Yousefi et al. (2021), there is no clear preferred model based on relative sea-level records in the region. Therefore, we create a composite average model, giving equal weight to a global lithospheric model, a regional lithospheric model, and a simple one-dimensional model. We include the variance between those models as additional uncertainty in the data covariance matrix, applying the influence of GIA as a correction (Fig. 2) to the data. Our locking model is fit to the surface deformation after removing the impact of GIA on that deformation. The average predicted uplift and subsidence pattern from these models is of a higher magnitude than identified in other work (Engelhart et al., 2015; Newton et al., 2021). Therefore, we also test a scaling factor on the GIA correction, from 0% to 125% of the Yousefi model-predicted range in modern GIA magnitude.

The on-going viscoelastic relaxation of the upper mantle throughout the earthquake cycle acts to increase deformation rates further inland. The data are therefore also likely impacted by ongoing viscoelastic effects. According to models by Li and Chen (2024), viscoelasticity causes changes in horizontal motions over time, defines the location of the pivot line between subsidence and uplift, as well as creates another secondary inland subsidence zone which cannot be predicted by elastic models. As the seismogenic zone of the Cascadia Subduction Zone is relatively shallow compared to other systems, we expect this viscoelastic variation, especially temporal variation, to be less pronounced than in subduction zones with wider seismogenic zones, and we expect viscoelasticity to primarily affect the far-field deformation pattern (Li et al., 2018; Li and Chen, 2023, 2024). Our correction thus only needs to account for the subsidence zone impacting the inland GNSS stations (Li and Chen, 2024).

Rather than fully modeling the viscoelastic signal, we apply a correction to the data. Correcting the data for this viscoelastic effect requires both a correction at GNSS stations and higher covariance due to uncertainty in the magnitude of that correction (Li et al., 2018). We estimate that correction (Fig. 2) by calculating the difference between the elastic and viscoelastic results for the preferred model from Li et al. (2018) (see Fig. 5 in publication). Since viscoelasticity of the upper mantle primarily impacts the stations farther inland, we apply this correction only to stations more than 50 km east of the coastline. It is at these eastern stations where the vertical data start to show subsidence that can't be replicated with an elastic model. As the pattern of the viscoelastic correction is similar to the GIA pattern, we test a similar scaling factor from 0% to 125% to look for a potential tradeoff between the two signals. The viscoelastic structure of the earth in this region has significant uncertainty, so we scale the uncertainty by the size of the viscoelastic signal.

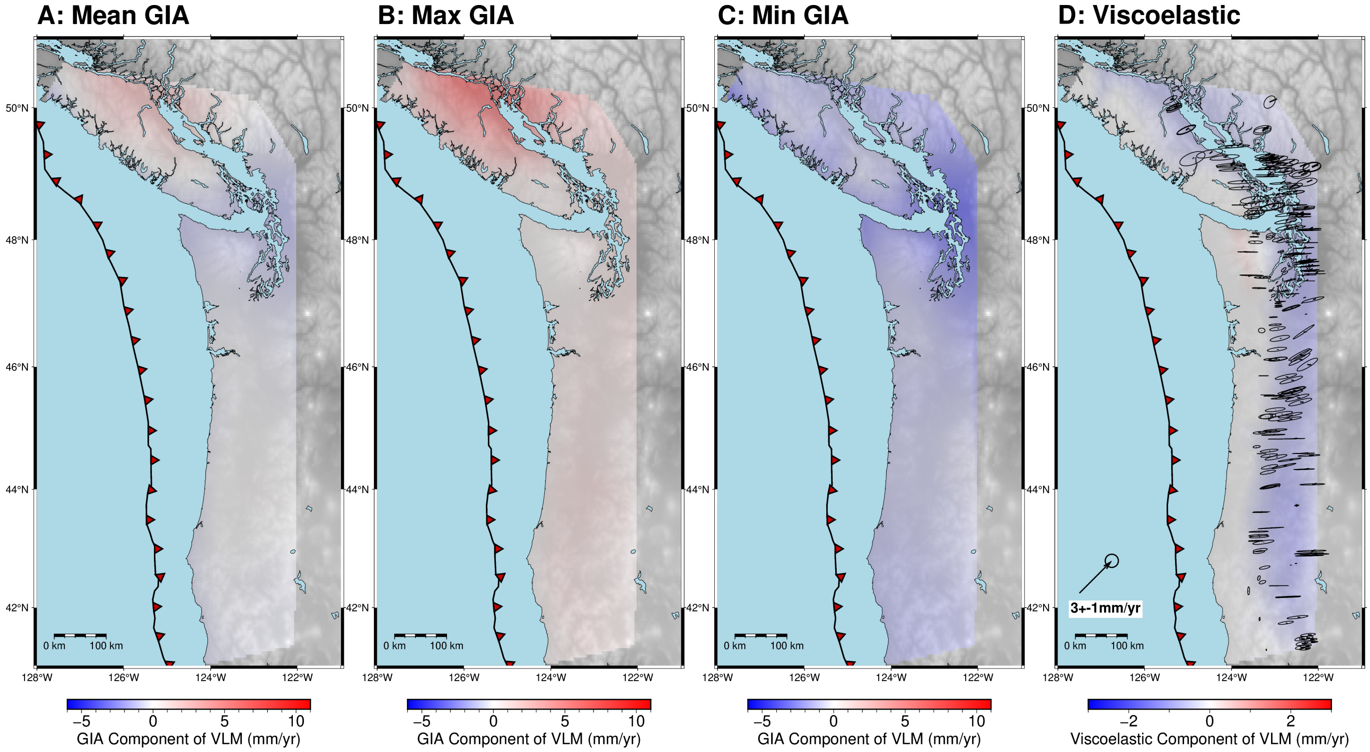

Figure 2 Maps of deformation patterns used to correct the data. (a) Mean impact of glacial isostatic adjustment (GIA) on vertical land movement (VLM) using composite model (Yousefi et al., 2021). (b) Maximum GIA impact of all models within the composite. (c) Minimum GIA impact of the same, showing how much the GIA prediction can vary depending on the viscosity structure and other choices made within the GIA model. (d) Viscoelastic correction (inferred from Li et al., 2018) applied to data (black arrows: horizontal velocities, shading: VLM).

2.3 Data Covariance Matrix

We construct a data covariance matrix, defined as the sum of the following terms: a diagonal matrix containing the initial measurement uncertainty, a correlation factor between data based on spatial proximity that affects the off-diagonal terms, and added uncertainties based on glacial isostatic adjustment and viscoelastic effects. Initial tests showed that the seafloor sites had little to no impact on the output locking models, due to the uncertainty in the seafloor data being much higher than the land-based GNSS stations. Despite the high uncertainties, we want the seafloor sites to contribute to the model, as they provide valuable new information about movement close to the deformation front. Therefore, we renormalize the uncertainties by dividing by a factor of 17 to bring the land and sea-based uncertainties into the same order-of-magnitude. This factor corresponds to the ratio of the mean GNSS-A uncertainty to the land GNSS uncertainty.

The construction of a stable, singular positive-definite data covariance matrix must be balanced with the need to have off-diagonal terms of the matrix that capture correlated surface velocity signals, which should not be attributed to spatial variations in locking on the fault. A positive definite matrix is necessary for Cholesky decomposition, a step used in the inversion process in order to speed up calculation of a correlated sample matrix. With larger off-diagonal terms, construction of a positive definite matrix becomes much less likely. In order to account for this issue, we construct the data covariance matrix by rescaling such that the off-diagonal elements are maximized and, when decomposed, all of the eigenvalues are above 5e-10 for numerical stability.

2.4 Inversion Methodology

Locking along a fault can be described as slip in the opposite direction of long-term plate motion, or backslip, representing the accumulation of elastic strain due to lack of fault slip (Savage, 1983). We formulate the backslip problem as a linear inverse of the observation equation $d=Gm$. We solve for locking along the subduction zone using an inversion of the data, d, to optimize the model parameters, m, corresponding to the backslip rates on the fault. G is a set of Green's functions for the relationship between a unit dislocation along each triangular element in our fault mesh in an elastic half-space and the associated deformation at the surface. The Green's functions are calculated using the program *TDdispHS* (Nikkhoo and Walter, 2015).

2.4.1 Bayesian approach

As the inversion setup is strongly non-unique, with many possible backslip patterns that fit the data, we use a Bayesian approach to derive a distribution of backslip magnitudes on each triangular element along the fault. We utilize the CATMIP algorithm (Minson et al., 2013) to solve for the posterior probability of the backslip distribution being true conditioned on the data $p\,(m_i|d)$ for each independent fault element, i. This is calculated

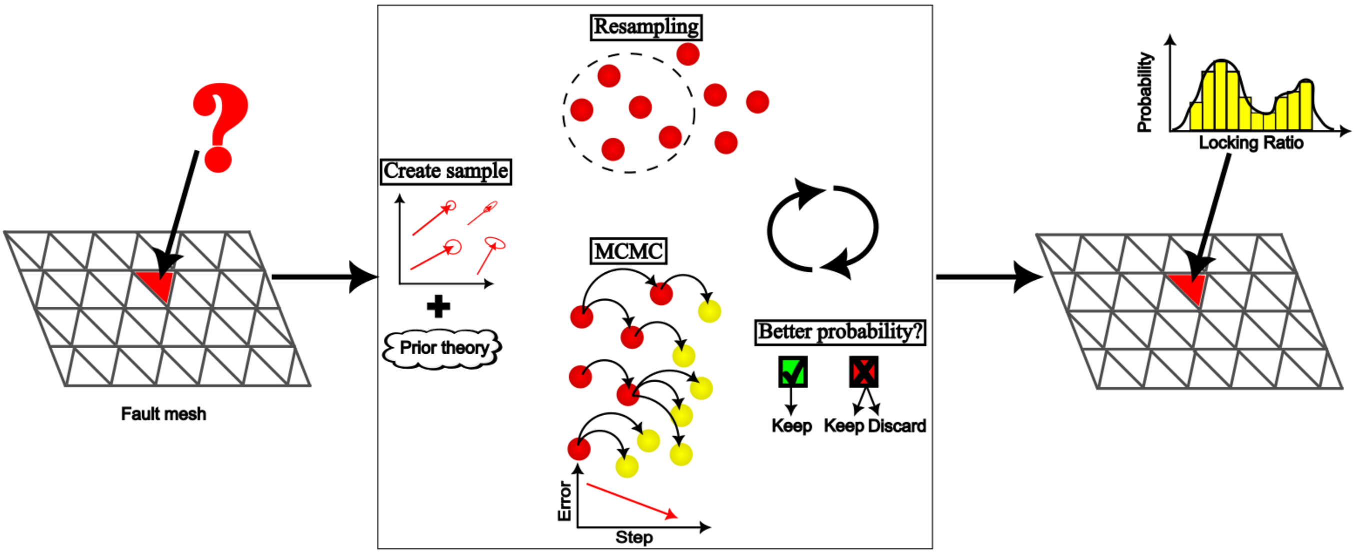

Figure 3 Schematic of CATMIP Bayesian inversion (Minson et al., 2013). For a fault element, create a sample of locking ratio values based on data and a prior locking assumption. Then, resample using the cooling rate and randomly explore the parameter space using Monte Carlo Markov Chains (MCMC). From the new sample, calculate the posterior probability. If it's improved, keep it, otherwise draw a random number to decide. The algorithm iterates, outputting a final distribution of locking ratios for that element.

based on the probability of observing the data, conditioned on a value for the prior, $p\left(d|m_i\right)$, which incorporates the data covariance matrix, and an *a priori* assumption of the backslip magnitude $p\left(m_i\right)$:

$$p\left(m_i|d\right) \;\propto\; p\left(d|m_i\right)p\left(m_i\right) \tag{1}$$

The algorithm requires several parameters controlling how the MCMC process is implemented. These include the number of chains within a single step, the length of the Markov chains, and the type of sampling method. We test the use of both a traditional Metropolis sampler and an adaptive Metropolis sampler, which considers a target acceptance rate and correlation value for the algorithm to check for after a specified number of updates to the Markov chain. We find no meaningful difference between the type of sampling method. We run our final model with 200 Markov chains at lengths of 5000 steps each, which ensures that the inversion fully explores the model space.

We assess the impact of using different priors *p(m)* within the inversion. To define a prior, we calculate the expected backslip rate on an element if the element is entirely locked, based on convergence vectors between the Juan De Fuca Plate and the Cascadia forearc. Next, we define a set of prior hypotheses about the associated backslip value on each element. For each fault element, we use truncated Gaussian prior distributions for the strike-slip and dip-slip components of fault slip, where the highest probability aligns with a given hypothesis about the locking pattern. These hypotheses can be informed by physical conditions, such as the thermal state, properties of the system, or end-member models. The suite of priors that we considered include completely creeping and completely locked plate interfaces, a gradual or abrupt transition between locked and creeping behavior at a particular depth, and examples of heterogeneous priors where transitions occur at particular latitudes along strike, including testing for variation that correlates with the boundaries of underlying terranes and presence of seamounts on the subducting plate (Table 1). We assess the success of different priors based on which ones achieve the lowest data misfit.

An example of a prior is shown in Figure S1, showing the mean values for the prior along the fault as well as several truncated Gaussian distributions for different elements. A detailed table outlining how we create these constraints can be found in Table S1, with an explanation for the parameter choices in the supplement. The shape of these distributions vary across the different elements along the fault, with changes along both the strike and dip directions (Fig. S1). The standard deviation of the input truncated Gaussian prior largely controls along-dip variations and the bounds of the truncated Gaussian prior primarily control along-strike variations (Fig. S1). The flexibility in these constraints allows the algorithm to iterate effectively while keeping the rake of the calculated backslip relatively close to the convergence vector between the two plates.

For display of each inversion result using a new set of parameters (Table 1), we convert the final output backslip magnitudes from the CATMIP algorithm to locking fractions by projecting the vectors onto the vector of the motion of convergence at that point (Wells and Simpson, 2014).

3 Results

3.1 Evaluation of preferred model

The Bayesian inversion returns the probability distribution of backslip on each fault element, *p(m|d)*. Each distribution can be characterized by a mean and standard deviation. The pattern of locking using the mean

Table 1 Set of model iterations tested within the algorithm, along with the choice of parameters for the best-fit model.

	Parameter	Variations	Best-Fit Variation	Goal
Model structure	Geometry	CASIE21 data (Carbotte et al., 2024) combined with McCrory et al. (2012), Slab 2.0 (Hayes et al., 2018), or Bloch et al. (2023)	Bloch et al. (2023)and CASIE21 data (Carbotte et al., 2024)	Smoothly incorporate the new shallow geometry
		10-50 km	40 km	Fit resolution of the data
	Data covariance matrix	Choice of what factors to include, relative magnitude of elements	Initial data uncertainty, spatial correlation, uncertainty from corrections, and scaling	Maximize off-diagonal elements, keep minimum eigenvalue above 5e-10
Corrections	Forearc rotation	Initial value (McCaffrey et al., 2007) or optimized rate	-1.57+/-0.02 *10-8 rad/year	Minimize misfit
	Magnitude of GIA correction	0% - 125% scaling factor on the initial pattern (Yousefi et al., 2021)	25%	
	Magnitude of viscoelastic correction	0% - 125% scaling factor on the initial pattern (Li et al., 2018)	75%	
Prior	Mean	Depth that locking starts (0-10 km)	0 km, changing to 80% locked past the deformation front	
		Depth that locking ends (20-30 km, variation along strike)	20km between the latitudes of 46°-48°, 25 km elsewhere	
		Smooth or abrupt change between creeping and locking	Abrupt	
		Variations depending on terrane or seamount presence	Not used	
	Uncertainty	See Table S1		

backslip for the preferred model suggests highly locked zones close to the deformation front (Fig. 4), with areas of especially high locking located immediately offshore the Olympic Peninsula. Moving down-dip beneath the coastline, the magnitude of locking is more moderate, although with a mean high enough for some locking to be occurring.

We chose a preferred model based on the parameters that yield the lowest misfit to the input data. The full list of parameters explored and the preferred parameters chosen are shown in Table 1. These optimized parameters include a 50% scaling factor on the GIA and a 25% scaling factor on the viscoelastic effect. The prior used in the preferred model assumes 100% locked at the deformation front, then steps down to 80% locked to a 25-kilometer depth (with a shallower depth of 20 km between the latitudes of 46°-48°) and 100% creeping below that depth. We also tested a prior with the same locking pattern but smoothed with depth, which produced a very similar result with no improvement to the fit (Table 1, Fig. S2d). The rotation rate is optimized during the inversion, giving a result of -1.57+/-0.02 $*10^{-8}$ rad/year, slightly slower than the -1.78$*10^{-8}$rad/year (clockwise) estimated by McCaffrey et al. (2007).

The residuals of the mean output model show a systematic pattern in some regions, especially inland (Fig. 5). The preferred model fits the horizontal and vertical data set with a R-squared value (coefficient of determination) of 0.91, indicating that 91% of the variation in the surface deformation can be fit with the model. The model underpredicts subsidence in inland Oregon and southern Washington as well as horizontal motion in some inland areas, most especially in the far north close to Vancouver, Canada. Overprediction of the horizontal motion occurs on Vancouver Island and the far southern region between 41°-42°. There are also some scattered points in the north that show observed uplift that is much higher than the modeled values. Other residuals are largely small, but systematic in some places.

Considering the full Bayesian result, spatially correlated locking models can be generated from the distribution of backslip on each fault element, indicating the range of model parameters that fit the data (Fig. S3). Rather than simply plotting the mean backslip rates, the backslip models in Fig. S3 are generated by subsampling the posterior backslip distributions assuming a spatial correlation between neighboring fault elements. These resampled distributions include models with more diffuse deeper locking in central Oregon or by a larger locked asperity offshore of the Olympic Peninsula. The range of locking ratios possible on each element varies in both the strike direction, with higher ranges of locking at the far northern end of the subduction zone, and the dip direction, with higher ranges in the shallower parts of the fault (Fig. 4b). The pattern of the standard deviation of the Bayesian result is consistent across a variety of models, suggesting that it mainly reflects how much flexibility there is in fitting the data, rather than being driven by the spread of the associated prior.

Despite the addition of new seafloor geodetic data, we do not see a reduction in the width of the posterior distributions in that area when using seafloor data. This is likely because station coverage is still much sparser towards the deformation front. It is possible to see an impact on distribution widths from including seafloor data, but only with an additional decrease in the seafloor data uncertainties by a factor of ten beyond the rescaling discussed in Section 2.3. As the number of observations increase and uncertainty goes down in the future, the contribution of seafloor data to constraining the locking distribution is expected to become increasingly significant.

3.2 Impact of GIA and Viscoelastic Data Corrections

Tests indicate a tradeoff between the magnitude of GIA and viscoelastic correction to the dataset. Both deformation sources contribute to inland subsidence, so a lower level of GIA correction is needed to improve the fit if a higher magnitude viscoelastic correction is incorporated (Fig. 6). The influence of the viscoelastic correction has a limited effect on the overall mean misfit, primarily impacting the fit to a small number of stations located in the Northern Cascades between the latitudes of about 48°-49° N. However, this correction greatly reduces systematic horizontal residuals in that region, in an area that is otherwise impossible to fit without locking as deep as 50 km. Residuals remain systematic to an extent in southern Washington and central Oregon, although at a much lower magnitude than the same model without data corrections (Fig. 6). This could indicate that a different glacial isostatic adjustment or viscoelastic effect pattern is necessary to improve the area of systematic residuals, as a stronger impact would improve this area but then fit worse when considering stations further south.

3.3 Impact of different priors

The balance between the structure of the data covariance matrix and prior (see Section 2.3) ensures that we minimize data misfit, which means that certain traits stay consistent in the model result, regardless of the *a priori* assumption. We see a similar depth for a decrease in average degree of locking at around 25 km (Fig. S2), regardless of whether the prior includes an assigned down-dip limit of locking or includes uniform locking at all depths. Therefore, a downdip decrease in locking is a robust feature.

While some model features remain stable, variations do emerge depending on the prior, particularly updip. Greater differences in the mean degree of locking occur when comparing priors that do or do not assume locking at the deformation front (Fig. S2). Heterogeneous priors, those incorporating variations based on terrane boundaries or subducting seamount locations, also have a small impact. These tend to slightly reduce the locking ratio near the deformation front, where data constraints are weaker, offset by a corresponding downdip increase in locking. The lowest misfit is achieved with a prior that assumes full locking at the deformation front and full creep below 20-25 km depth,

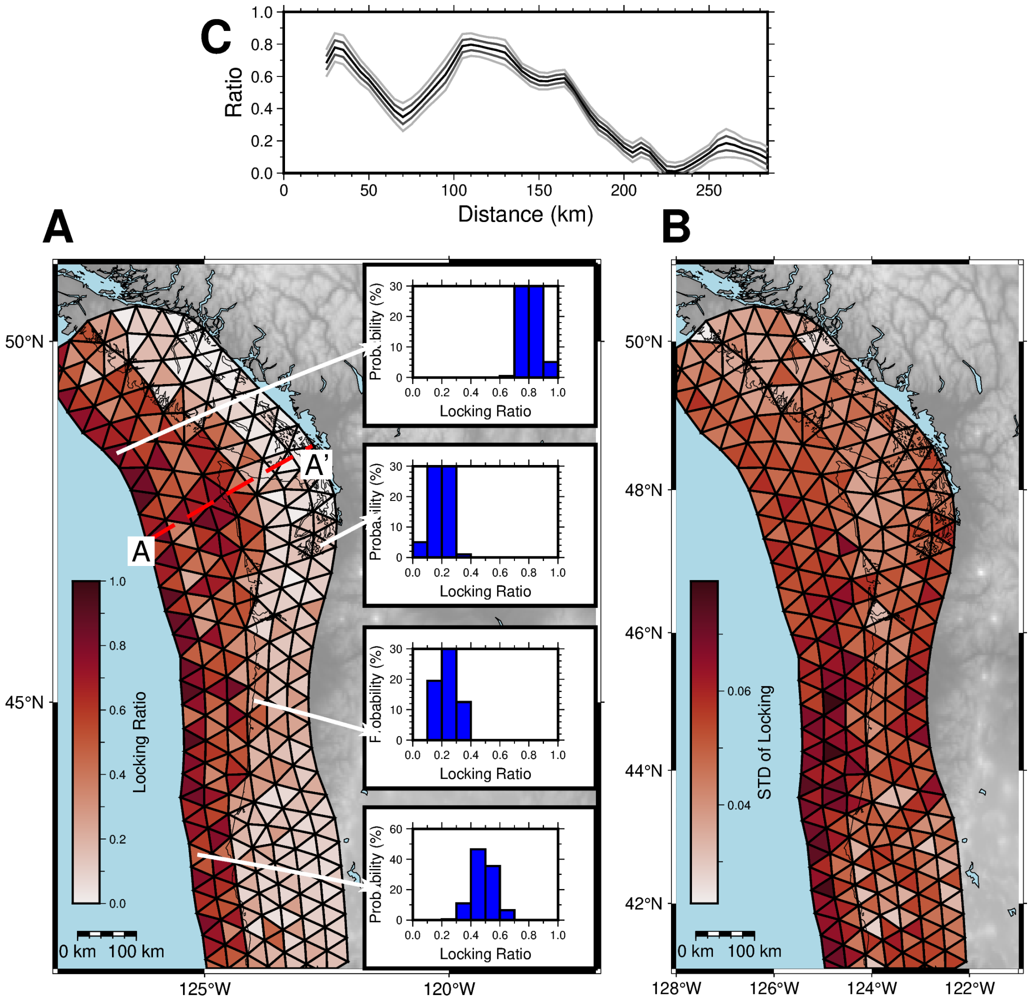

Figure 4 Posterior distributions of locking models conditioned on the data, p(m|d). (a) Mean locking ratio along the plate interface, with inset histograms of distribution for four fault elements and cross-section line A-A'. (b) Standard deviation of locking ratio, (c) Cross-section along A-A' showing the mean (black), σ(dark gray), and 2σ(light gray) of the locking ratio.

suggesting that this prior may best represent conditions on the fault.

3.4 Impact of other factors

We also test the impact of changes in the model structure and dataset on the results. We use an updated geometry source for the offshore portion of the fault using the CASIE21 data (Carbotte et al., 2024). This results in a flatter and shallower offshore fault geometry, with an associated decrease in the predicted locking in order to match the on-shore motion.

With the addition of several seafloor geodetic stations, we also see some disagreement between on and offshore data. The seafloor stations are best fit with 100% locking in that area, but this results in overprediction of motion at the coast in this area. This may indicate that the model is unable to fully resolve a very narrow offshore band of complete locking, or that inelastic or heterogenous rheology is required.

Using the rotation rate calculated by McCaffrey et al. (2007), we see a systematic rotational signal in the residuals (Fig. S4), with similar results regardless of prior or magnitude of corrections. When the rotation rate is included as a free model parameter, the inversion prefers a lower rate. This result is consistent across different priors, suggesting that, when considering the impact of these other factors, the amount of forearc rotation may be lower.

4 Discussion

4.1 Assessment of locking pattern

Past deterministic locking models use a fundamentally different approach to our Bayesian inversion. However, they offer useful benchmarks for comparison, both in terms of shared features in our mean locking patterns as well as highlighting the broader range of plausible solutions in our probabilistic framework. Several aspects of the overall mean locking ratio pattern show similarity with previous studies, including a high probability of locking at the deformation front and a decrease in the mean locking at approximately around 20-25 km depth along most of the fault (e.g. Li et al., 2018; McCaffrey et al., 2013; Schmalzle et al., 2014). We also find that some locking fractions allowed within the distributions show a strong asperity patch offshore of the Olympic Peninsula, in accordance with previous work, although this does not appear in the full range of possible locking models. The overall pattern of the mean locking ratios (Fig. 4) shows considerable roughness, which is

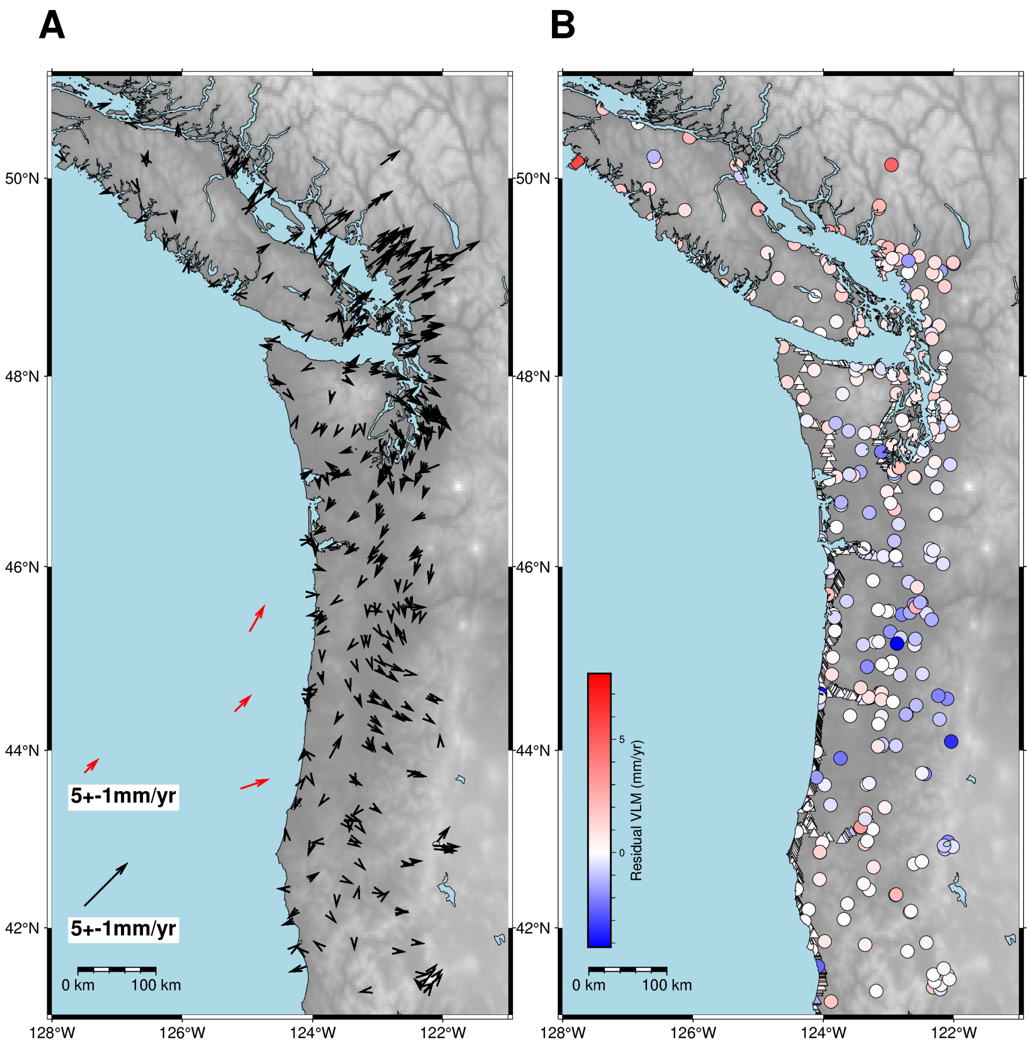

Figure 5 (a) Residual horizontal velocities for the mean locking ratio (predictions from the model subtracted from the observed data), compared to data uncertainties (circles). (b) Residual vertical velocities for the mean locking ratio.

not unexpected in a situation in which smoothing is not explicitly imposed within the inversion (Minson et al., 2014). The roughness could represent undersampling, but increasing the number of samples does not change the variability of the means or model posterior roughness (Fig. S5). The off-diagonal terms of the data covariance matrix define the *a priori* covariances and impact the degree of spatial smoothness in the means of the resulting posterior models, which must be balanced along with constructing a stable data covariance matrix (see Section 2.3). The ensemble of models (Fig. S3) provides a clearer picture of the underlying variability.

Some spatial variance in the mean is to be expected in a probabilistic framework. The variance of the mean locking ratio on adjacent fault patches is not necessarily significant on their own, but rather reflect the range of solutions within the probabilistic framework. The span of possible locking models that fit the data (Fig. S3) indicates that there is considerable variation in potential locking patterns, given existing data and the inherent non-uniqueness of the problem. Approximately half of all pairs of nearby patches are within one standard deviation of each other and 70% are within two standard deviations of each other. There is more disagreement between neighboring fault patches in the northern third of the fault model, which may be related to the model setup or the distribution of GNSS sites. The apparent combination of rough mean structure and locally low uncertainty in the posterior distributions is a recognized behavior in Bayesian sampling approaches without explicit smoothing (e.g., Minson et al., 2014; Nocquet, 2018).

An examination of data residuals suggests that our model continues to show some areas for improvement. There are coherent vertical residuals for the model due to insufficient subsidence predicted by the model in Central Oregon and a few scattered very high magnitude values showing insufficient uplift in the north. This may suggest that the pattern of GIA, based upon an average of several existing GIA models (Yousefi et al., 2021), is not entirely accurate. These models already vary in their latitudinal pattern, and an adjusted model might explain some of these coherent residuals. The small areas of coherent horizontal residuals in the northern Cascades and in the region between a latitude of 46°-48°, which could be similarly impacted by variation in the model of GIA and viscoelastic effects.

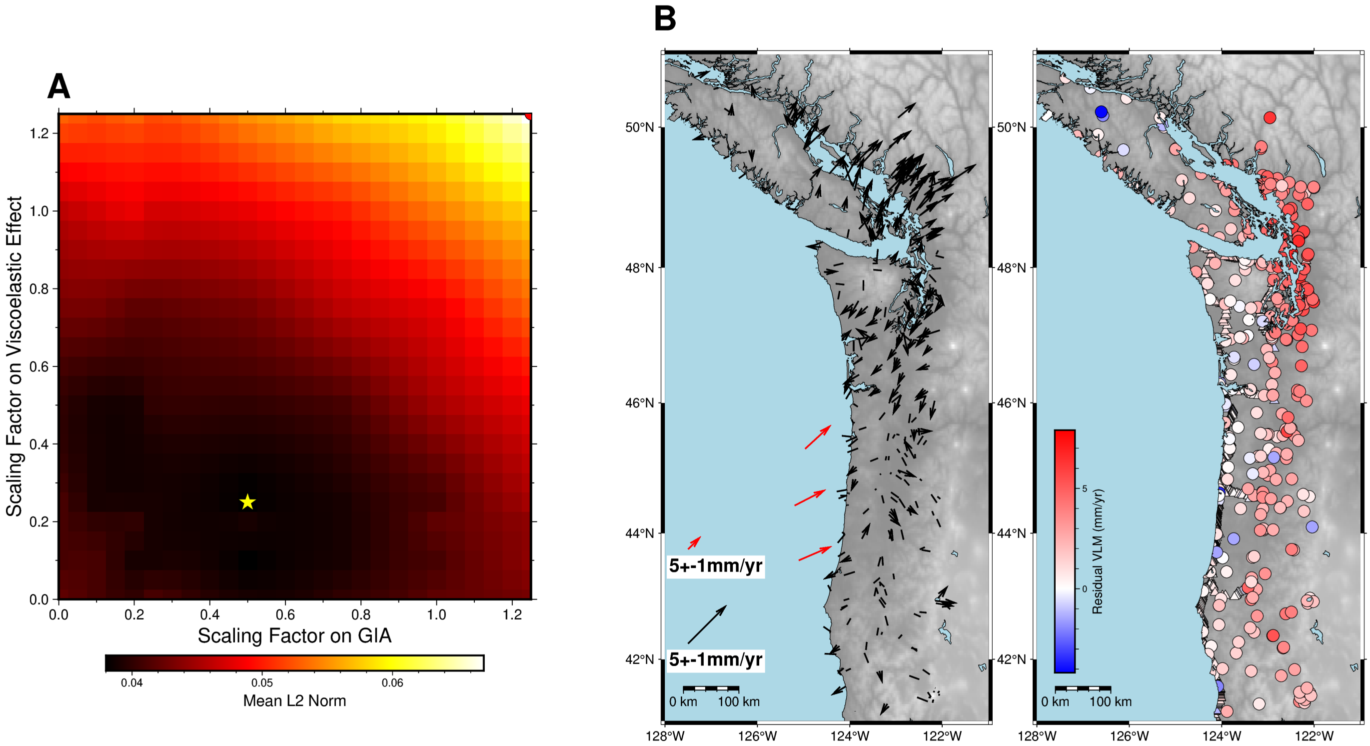

Figure 6 (a). Scaling of the data corrections, showing the tradeoff between GIA and viscoelastic data corrections. Contours show overall data misfit (contours) for each iteration of the Bayesian Inversion with different magnitudes of GIA and viscoelastic contributions (black dots). Yellow star is the model with the best fit (residuals in Fig. 5), red circle is the model with the worst fit (residuals in b). (b) Horizontal and vertical residuals for the worst model run.

4.2 Data corrections

The data are consistently better fit by a magnitude of GIA correction that is lower than the average magnitude predicted by the Yousefi models, in agreement with other work that has suggested a lower overall magnitude of the modern-day GIA signal (Engelhart et al., 2015; Newton et al., 2021). We estimate that the combination of the GIA and viscoelastic signal must be relatively small, at a maximum of 3.5 mm/yr of vertical subsidence based on scaling factors from our preferred model, in contrast with some existing models (Yousefi et al., 2021). However, both the horizontal and vertical data are also far better fit with the inclusion of GIA and viscoelastic corrections, in comparison with an uncorrected model (Fig. 6). This suggests that these processes are regionally influential on the deformation pattern in Cascadia, and should be considered in future work focused on regional deformation. This approach of applying and scaling the corrections was effective at quantifying the range of different factors and estimating their isolated impact on surface deformation. However, the tradeoff in improved fit between the GIA and viscoelastic corrections indicates that uncertainty in the regional Earth structure is currently limiting our ability to quantify their relative impact. This work and similar analyses would benefit from better constrained measurements of Earth structure.

4.3 Probabilistic approach

The use of a Bayesian approach to the inversion, implementing the CATMIP algorithm, results in a thorough assessment of the range of locking patterns that fit the available data in Cascadia. The use of a prior allows us to explicitly test hypotheses about the locking pattern, by evaluating how the algorithm minimizes data misfit in each case. However, our work also highlights the sensitivity of the probabilistic approach to *a priori* assumptions and the construction of the data covariance matrix. Changes to the model structure required careful balancing of the magnitude of uncertainty in the prior and data covariance matrix in order to fulfill two objectives. First, we needed to ensure that the algorithm could converge to a result that minimized data misfit, which reflects the importance of the data. Second, we needed to allow the prior itself to contribute some guidance to the algorithm in areas where there is sufficient data uncertainty, which reflects the importance of our *a priori* assumption based on physical attributes (Flück et al., 1997; Han et al., 2017; Seyler et al., 2020).

4.4 Significance

We find that a Bayesian elastic locking model can explain the pattern of surface deformation in Cascadia, including the pattern seen in both the horizontal and vertical data. Common patterns within the probabilistic locking model highlight where elastic strain is accumulating in the crust and could be released in a future earthquake, with strong locking towards the deformation front as well as a possible asperity offshore of the Olympic Peninsula. However, the locking models do imply a high probability of low locking deeper than 20 km depth and associated reduced risk of higher inland ground shaking from contemporary loading (Wirth et al., 2018). The output also suggests potential heterogeneity of the locked zone along strike.

Our work also has implications for locking models in regions outside of the Cascadia Subduction Zone. The use of a probabilistic approach provides a thorough exploration of the set of possible models that fit the data. The range of distributions we find in our results highlights where a deterministic locking model would have missed the full range and potentially indicated a level of certainty not reflected by the data. Our results also stress the importance of seafloor geodetic data to estimating locking, as their inclusion within our model brought to light that the model has difficulty fitting both coastal and offshore data in that area.

5 Conclusion

A Bayesian locking model for the Cascadia Subduction Zone is consistent with horizontal and vertical geodetic data in the region. The use of a prior based on full offshore locking and a transition to creep at around 20-25 km depth aligns with the lowest data misfit, reinforcing existing constraints of offshore locking found in previous studies (e.g. Li et al., 2018; McCaffrey et al., 2013; Schmalzle et al., 2014). While glacial isostatic adjustment and viscoelastic effects provide second-order improvements in model fit, the primary deformation signal remains dominated by elastic locking. Using a probabilistic approach, the range of locking models reveals significant uncertainty in the range of potential locking patterns, in spite of the inclusion of seafloor geodetic data improving the data constraints. This suggests that heterogeneity in strain accumulation in Cascadia, and its association with seismic hazards, still has significant uncertainty and comprehensive seismic hazard assessments must account for the range of possible slip distributions. Addressing this uncertainty also requires continued refinement of geodetic observations, especially at the seafloor, and improved Earth structure models that help to refine the impact of effects like glacial isostatic adjustment.

Acknowledgements

The authors would like to thank Sarah Minson for discussions on the use of CATMIP and two reviewers, Eric Lindsey and Kaj Johnson, for their helpful comments. Support has been provided by the National Science Foundation (OCE-2127140 and COPE-2103713).

Data availability

GNSS data was pulled from Newton et al. (2021), as provided by the following GNSS processing centers: UNR (http://geodesy.unr.edu), JPL (https://sideshow.jpl.nasa.gov/pub/), SOPAC (http://garner.ucsd.edu/pub), and PANGA (http://www.geodesy.cwu.edu/panga) , as well as seafloor GNSS-A data from DeSanto et al. (2025). The spirit leveling data was derived from Newton et al. (2021) and Patton et al. (2023). The amalgamated dataset used in this paper, extended south from the original Newton et al. (2021) paper and including a list of the excluded sites, is provided as a part of the code input files.

Fault geometry was calculated from Bloch et al. (2023) and CASIE21 data (Carbotte et al., 2024). The GIA models are available from Yousefi et al. (2021) and the viscoelastic models come from Li et al. (2018).

The Bayesian inversion code is available from GitHub (https://github.com/AlTarFramework/altar). The merged fault model and posterior distributions from the preferred model, along with input files used for the code (combined GNSS and leveling dataset, Green's functions matrix, and data covariance matrix), are available at Pearson and Schmidt (2026).

Competing interests

The authors have no competing interests.

References

Blewitt, G., Hammond, W., and Kreemer, C. Harnessing the GPS Data Explosion for Interdisciplinary Science. *Eos*, 99, 2018. doi: 10.1029/2018eo104623.

Bloch, W., Bostock, M. G., and Audet, P. A Cascadia Slab Model From Receiver Functions. *Geochemistry, Geophysics, Geosystems*, 24(10), Oct. 2023. doi: 10.1029/2023gc011088.

Carbotte, S. M., Boston, B., Han, S., Shuck, B., Beeson, J., Canales, J. P., Tobin, H., Miller, N., Nedimovic, M., Tréhu, A., Lee, M., Lucas, M. C., Jian, H., Jiang, D., Moser, L., Anderson, C., Judd, D., Fernandez, J., Campbell, C., Goswami, A., and Gahlawat, R. Subducting plate structure and megathrust morphology from deep seismic imaging linked to earthquake rupture segmentation at Cascadia. *Science Advances*, 10(23), 2024. doi: 10.1126/sciadv.adl3198.

Clark, J., Mitrovica, J. X., and Latychev, K. Glacial isostatic adjustment in central Cascadia: Insights from three-dimensional Earth modeling. *Geology*, 47(4):295–298, Feb. 2019. doi: 10.1130/g45566.1.

Coreform LLC. Coreform Cubit. Computer software, 2018. http://coreform.com. Version 2021.5.

Dal Zilio, L., Jolivet, R., and van Dinther, Y. Segmentation of the Main Himalayan Thrust Illuminated by Bayesian Inference of Interseismic Coupling. *Geophysical Research Letters*, 47(4), Feb. 2020. doi: 10.1029/2019gl086424.

DeSanto, J. B., Schmidt, D. A., Zumberge, M., Sasagawa, G., and Chadwell, C. D. Near full locking on the shallow megathrust of the central Cascadia subduction zone revealed by GNSS-Acoustic. *Earth and Planetary Science Letters*, 665, 2025. doi: 10.1016/j.epsl.2025.119463.

Engelhart, S. E., Vacchi, M., Horton, B. P., Nelson, A. R., and Kopp, R. E. A sea-level database for the Pacific coast of central North America. *Quaternary Science Reviews*, 113:78–92, Apr. 2015. doi: 10.1016/j.quascirev.2014.12.001.

Flück, P., Hyndman, R. D., and Wang, K. Three-dimensional dislocation model for great earthquakes of the Cascadia Subduction Zone. *Journal of Geophysical Research: Solid Earth*, 102(B9), 1997. doi: 10.1029/97jb01642.

Han, S., Bangs, N. L., Carbotte, S. M., Saffer, D. M., and Gibson, J. C. Links between sediment consolidation and Cascadia megathrust slip behaviour. *Nature Geoscience*, 10(12):954–959, Nov. 2017. doi: 10.1038/s41561-017-0007-2.

Hayes, G. P., Moore, G. L., Portner, D. E., Hearne, M., Flamme, H., Furtney, M., and Smoczyk, G. M. Slab2, a comprehensive subduction zone geometry model. *Science*, 362(6410):58–61, Oct. 2018. doi: 10.1126/science.aat4723.

Jamason, P., Bock, Y., Fang, P., Gilmore, B., Malveaux, D., Prawirodirdjo, L., and Scharber, M. SOPAC Web site (http://-sopac.ucsd.edu). *GPS Solutions*, 8(4):272–277, Oct. 2004. doi: 10.1007/s10291-004-0118-2.

Kemp, A. C., Cahill, N., Engelhart, S. E., Hawkes, A. D., and Wang, K. Revising Estimates of Spatially Variable Subsidence during the A.D. 1700 Cascadia Earthquake Using a Bayesian Foraminiferal Transfer Function. *Bulletin of the Seismological Society of America*, 108(2):654–673, Mar. 2018. doi: 10.1785/0120170269.

Konca, A. O., Avouac, J.-P., Sladen, A., Meltzner, A. J., Sieh, K., Fang, P., Li, Z., Galetzka, J., Genrich, J., Chlieh, M., Natawidjaja, D. H., Bock, Y., Fielding, E. J., Ji, C., and Helmberger, D. V. Partial rupture of a locked patch of the Sumatra megathrust during the 2007 earthquake sequence. *Nature*, 456(7222):631–635, Dec. 2008. doi: 10.1038/nature07572.

Li, S. and Chen, L. How Long Can the Postseismic and Interseismic Phases of Great Subduction Earthquake Sustain? Toward an Integrated Earthquake-Cycle Perspective. *Geophysical Research Letters*, 50(11), 2023. doi: 10.1029/2023gl103976.

Li, S. and Chen, L. Vertical Crustal Deformation Due To Viscoelastic Earthquake Cycles at Subduction Zones: Implications for Nankai and Cascadia. *Journal of Geophysical Research: Solid Earth*, 129(8), Aug. 2024. doi: 10.1029/2024jb028817.

Li, S., Wang, K., Wang, Y., Jiang, Y., and Dosso, S. E. Geodetically Inferred Locking State of the Cascadia Megathrust Based on a Viscoelastic Earth Model. *Journal of Geophysical Research: Solid Earth*, 123(9), 2018. doi: 10.1029/2018jb015620.

Li, S., Fukuda, J., and Oncken, O. Geodetic Evidence of Time-Dependent Viscoelastic Interseismic Deformation Driven by Megathrust Locking in the Southwest Japan Subduction Zone. *Geophysical Research Letters*, 47(4), Feb. 2020. doi: 10.1029/2019gl085551.

Lindsey, E. O., Mallick, R., Hubbard, J. A., Bradley, K. E., Almeida, R. V., Moore, J. D. P., Bürgmann, R., and Hill, E. M. Slip rate deficit and earthquake potential on shallow megathrusts. *Nature Geoscience*, 14(5):321–326, May 2021. doi: 10.1038/s41561-021-00736-x.

Lorito, S., Romano, F., Atzori, S., Tong, X., Avallone, A., McCloskey, J., Cocco, M., Boschi, E., and Piatanesi, A. Limited overlap between the seismic gap and coseismic slip of the great 2010 Chile earthquake. *Nature Geoscience*, 4(3):173–177, Jan. 2011. doi: 10.1038/ngeo1073.

Loveless, J. P. and Meade, B. J. Spatial correlation of interseismic coupling and coseismic rupture extent of the 2011 M_W= 9.0 Tohoku-oki earthquake: COUPLING AND TOHOKU-OKI SLIP. *Geophysical Research Letters*, 38(17), 2011. doi: 10.1029/2011gl048561.

Matsu'ura, M., Noda, A., and Fukahata, Y. Geodetic data inversion based on Bayesian formulation with direct and indirect prior information: Geodetic data inversion based on Bayesian formulation. *Geophysical Journal International*, 171(3), 2007. doi: 10.1111/j.1365-246x.2007.03578.x.

McCaffrey, R., Qamar, A. I., King, R. W., Wells, R., Khazaradze, G., Williams, C. A., Stevens, C. W., Vollick, J. J., and Zwick, P. C. Fault locking, block rotation and crustal deformation in the Pacific Northwest. *Geophysical Journal International*, 169(3), 2007. doi: 10.1111/j.1365-246x.2007.03371.x.

McCaffrey, R., King, R. W., Payne, S. J., and Lancaster, M. Active tectonics of northwestern U.S. inferred from GPS-derived surface velocities. *Journal of Geophysical Research: Solid Earth*, 118(2): 709–723, Feb. 2013. doi: 10.1029/2012jb009473.

McCrory, P. A., Blair, J. L., Waldhauser, F., and Oppenheimer, D. H. Juan de Fuca slab geometry and its relation to Wadati-Benioff zone seismicity. *Journal of Geophysical Research: Solid Earth*, 117(B9), 2012. doi: 10.1029/2012jb009407.

Miller, M., Johnson, D., Rubin, C., Dragert, H., Endo, E., and Humphreys, E. GPS monitoring of the Cascadia Margin: The Pacific Northwest Geodetic Array (PANGA). *Eos Trans AGU*, 78:46, 1997.

Minson, S. E., Simons, M., and Beck, J. L. Bayesian inversion for finite fault earthquake source models I—theory and algorithm. *Geophysical Journal International*, 194(3), 2013. doi: 10.1093/gji/ggt180.

Minson, S. E., Simons, M., Beck, J. L., Ortega, F., Jiang, J., Owen, S. E., Moore, A. W., Inbal, A., and Sladen, A. Bayesian inversion for finite fault earthquake source models – II: the 2011 great Tohoku-oki, Japan earthquake. *Geophysical Journal International*, 198(2), 2014. doi: 10.1093/gji/ggu170.

Métois, M., Socquet, A., and Vigny, C. Interseismic coupling, segmentation and mechanical behavior of the central Chile subduction zone. *Journal of Geophysical Research: Solid Earth*, 117 (B3), Mar. 2012. doi: 10.1029/2011jb008736.

Nalbant, S., McCloskey, J., Steacy, S., NicBhloscaidh, M., and Murphy, S. Interseismic coupling, stress evolution, and earthquake slip on the Sunda megathrust. *Geophysical Research Letters*, 40 (16):4204–4208, Aug. 2013. doi: 10.1002/grl.50776.

Newton, T., Weldon, R., Miller, I., Schmidt, D., Mauger, G., Morgan, H., and Grossman, E. An Assessment of Vertical Land Movement to Support Coastal Hazards Planning in Washington State. *Water*, 13(3):281, Jan. 2021. doi: 10.3390/w13030281.

Nikkhoo, M. and Walter, T. R. Triangular dislocation: an analytical, artefact-free solution. *Geophysical Journal International*, 201(2):1119–1141, Mar. 2015. doi: 10.1093/gji/ggv035.

Nocquet, J.-M. Stochastic static fault slip inversion from geodetic data with non-negativity and bound constraints. *Geophysical Journal International*, 214(1):366–385, Apr. 2018. doi: 10.1093/gji/ggy146.

Patton, J., Williams, T., Anderson, J., Hemphill-Haley, M., Burgette, R., Weldon II, R., McPherson, R., and Leroy, T. 20th to 21st century relative sea and land level changes in Northern California: Tectonic land level changes and their contribution to sea-level rise. *Tektonika*, 1(1), 2023. doi: 10.55575/tektonika2023.1.1.6.

Pearson, A. E. R. and Schmidt, D. Datasets associated with the publication The Distribution of Interseismic Locking on the Cascadia Subduction Zone Using Bayesian Methods, July 2026. doi: 10.5281/zenodo.21479776.

Pollitz, F. F. 3D Viscoelastic Models of Slip-Deficit Rate Along the Cascadia Subduction Zone. *Journal of Geophysical Research: Solid Earth*, 130(1), Jan. 2025. doi: 10.1029/2024jb029847.

Protti, M., González, V., Newman, A. V., Dixon, T. H., Schwartz, S. Y., Marshall, J. S., Feng, L., Walter, J. I., Malservisi, R., and Owen, S. E. Nicoya earthquake rupture anticipated by geodetic measurement of the locked plate interface. *Nature Geoscience*, 7(2): 117–121, Dec. 2013. doi: 10.1038/ngeo2038.

Satake, K., Shimazaki, K., Tsuji, Y., and Ueda, K. Time and size of a giant earthquake in Cascadia inferred from Japanese tsunami records of January 1700. *Nature*, 379(6562):246–249, Jan. 1996. doi: 10.1038/379246a0.

Sato, D. S., Hori, T., and Fukahata, Y. Differentiating Frictionally Locked Asperities From Kinematically Coupled Zones. *Journal of Geophysical Research: Solid Earth*, 130(10), Oct. 2025. doi: 10.1029/2024jb030357.

Savage, J. C. A dislocation model of strain accumulation and release at a subduction zone. *Journal of Geophysical Research: Solid Earth*, 88(B6), 1983. doi: 10.1029/jb088ib06p04984.

Savage, J. C., Svarc, J. L., Prescott, W. H., and Murray, M. H. Deformation across the forearc of the Cascadia subduction zone at Cape Blanco, Oregon. *Journal of Geophysical Research: Solid Earth*, 105(B2):3095–3102, Feb. 2000. doi: 10.1029/1999jb900392.

Schmalzle, G. M., McCaffrey, R., and Creager, K. C. Central Cascadia subduction zone creep. *Geochemistry, Geophysics, Geosystems*, 15(4):1515–1532, Apr. 2014. doi: 10.1002/2013gc005172.

Seyler, C., Kirkpatrick, J., Savage, H., Hirose, T., and Faulkner, D. Rupture to the trench? Frictional properties and fracture energy of incoming sediments at the Cascadia subduction zone. *Earth and Planetary Science Letters*, 546, 2020. doi: 10.1016/j.epsl.2020.116413.

Sherrill, E. M., Johnson, K. M., and Jackson, N. M. Locating Boundaries Between Locked and Creeping Regions at Nankai and Cascadia Subduction Zones. *Journal of Geophysical Research: Solid Earth*, 129(10), Oct. 2024. doi: 10.1029/2024jb029346.

Shirzaei, M., Freymueller, J., Törnqvist, T. E., Galloway, D. L., Dura, T., and Minderhoud, P. S. J. Measuring, modelling and projecting coastal land subsidence. *Nature Reviews Earth & Environment*, 2 (1):40–58, Dec. 2020. doi: 10.1038/s43017-020-00115-x.

Thatcher, W. The earthquake deformation cycle at the Nankai Trough, southwest Japan. *Journal of Geophysical Research: Solid Earth*, 89(B5):3087–3101, May 1984. doi: 10.1029/jb089ib05p03087.

Wang, K. and Tréhu, A. M. Invited review paper: Some outstanding issues in the study of great megathrust earthquakes—The Cascadia example. *Journal of Geodynamics*, 98:1–18, Aug. 2016. doi: 10.1016/j.jog.2016.03.010.

Wang, K., Hu, Y., and He, J. Deformation cycles of subduction earthquakes in a viscoelastic Earth. *Nature*, 484(7394):327–332, Apr. 2012. doi: 10.1038/nature11032.

Wang, P., Engelhart, S. E., Wang, K., Hawkes, A. D., Horton, B. P., Nelson, A. R., and Witter, R. C. Heterogeneous rupture in the great Cascadia earthquake of 1700 inferred from coastal subsidence estimates. *Journal of Geophysical Research: Solid Earth*, 118(5):2460–2473, May 2013. doi: 10.1002/jgrb.50101.

Wells, R. E. and McCaffrey, R. Steady rotation of the Cascade arc. *Geology*, 41(9), 2013. doi: 10.1130/g34514.1.

Wells, R. E. and Simpson, R. W. Northward migration of the Cascadia forearc in the northwestern U.S. and implications for subduction deformation. *Earth, Planets and Space*, 53(4), 2014. doi: 10.1186/bf03352384.

Wirth, E. A. and Frankel, A. D. Impact of Down-Dip Rupture Limit and High-Stress Drop Subevents on Coseismic Land-Level Change during Cascadia Megathrust Earthquakes. *Bulletin of the Seismological Society of America*, 109(6):2187–2197, Oct. 2019. doi: 10.1785/0120190043.

Wirth, E. A., Frankel, A. D., Marafi, N., Vidale, J. E., and Stephenson, W. J. Broadband Synthetic Seismograms for Magnitude 9 Earthquakes on the Cascadia Megathrust Based on 3D Simulations and Stochastic Synthetics, Part 2: Rupture Parameters and Variability. *Bulletin of the Seismological Society of America*, 108 (5A):2370–2388, Aug. 2018. doi: 10.1785/0120180029.

Yousefi, M., Milne, G. A., and Latychev, K. Glacial isostatic adjustment of the Pacific Coast of North America: the influence of lateral Earth structure. *Geophysical Journal International*, 226(1): 91–113, Feb. 2021. doi: 10.1093/gji/ggab053.

Zumberge, J. F. Automated GPS Data Analysis Service. *GPS Solutions*, 2(3):76–78, Jan. 1999. doi: 10.1007/pl00012760.